Surprisingly large anomalous Hall effect and giant negative magnetoresistance in half-topological semimetals

Yanglin Zhu[1,2+], Cheng-Yi Huang[3+], Yu Wang[1], David Graf [4], Hsin Lin[5], Seng Huat Lee[1], John Singleton[6], Lujin Min[1], Johanna C. Palmstrom[6], Arun Bansil[3], Bahadur Singh[7*], and Zhiqiang Mao[1*]

[1] Department of Physics, Pennsylvania State University, University Park, PA, 16802

[2] School of Physics and Technology, Nanjing Normal University, Nanjing, China, 210046

[3] Department of Physics, Northeastern University, Boston, USA, 02115

[4] National High Magnetic Field Laboratory, Tallahassee, FL, 32310

[5] Institute of Physics, Academia Sinica, Taipei 11529, Taiwan

[6] National High Magnetic Field Laboratory, Pulse Field Facility, Los Alamos National Laboratory, Los Alamos, NM, 87545

[7] Department of Condensed Matter Physics and Materials Science, Tata Institute of Fundamental Research, Mumbai 400005, India

Abstract

Proposed mechanisms for large intrinsic anomalous Hall effect (AHE) in magnetic topological semimetals include diverging Berry curvatures of Weyl nodes, anticrossing nodal rings or points of non-trivial bands, etc. Here we demonstrate that a half-topological semimetal (HTS) state near a topological critical point can provide a new mechanism for an exceptionally large AHE via systematic studies on an antiferromagnetic (AFM) half-Heusler compound TbPdBi. We not only observe a surprisingly large AHE with $\tan\Theta^{H} \approx 2$ in its field-driven ferromagnetic (FM) phase, but also find a distinct Hall resistivity peak in its canted AFM phase. Moreover, we observe a giant negative magnetoresistance with a value of ~98%. Our in-depth theoretical modelling indicates that these exotic transport properties originate from the HTS state which exhibits Berry curvature cancellation between the trivial spin-up

and nontrivial spin-down bands . Our study offers new strategies for improved materials design for spintronics and other applications.

+These two authors equally contribute to this work.

*emails: bahadur.singh@tifr.res.in, zim1@psu.edu

a. Introduction

Large intrinsic anomalous Hall effect (AHE) in topological semimetals has been a subject of intensive studies. Unlike the conventional Hall effect, which is caused by the Lorentz force under an external magnetic field, the intrinsic AHE stems from the net Berry curvature $\boldsymbol{\Omega}(k)$ associated with the electronic bands [1-3]. $\boldsymbol{\Omega}(k)$, which describes the geometry of the Bloch wavefunctions, is determined by the topology of the band structure. When a longitudinal electric field is applied, $\boldsymbol{\Omega}(k)$ imparts transverse velocity [$\propto \boldsymbol{E} \times \boldsymbol{\Omega}(k)$] to Bloch electrons and thus results in the AHE. Presence of an intrinsic AHE requires time-reversal symmetry (TRS) to be broken. Therefore, large intrinsic AHE is usually expected in magnetic materials with Berry curvature hot spots near the Fermi level. Prior studies have found that several types of magnetic topological materials can exhibit large intrinsic AHE. These include ferromagnetic (FM) Weyl semimetals such as $Co_3Sn_2S_2$ [4,5] and Co_2MnGa [6,7], which host Weyl nodal crossings that lie close to the Fermi level and carry a diverging Berry curvature. With the TRS broken by ferromagnetism, the Berry curvature contribution from the Weyl nodes with opposite chirality will not cancel out, resulting in a large AHE. Strength of the AHE is usually characterized by the intrinsic anomalous Hall angle (AHA) Θ^{H}, where $\Theta^{H} = \tan^{-1}(\sigma_{yx}^{AH}/\sigma_{xx})$, and σ_{yx}^{AH} and σ_{xx} are the anomalous Hall conductivity and longitudinal conductivity, respectively. $Co_3Sn_2S_2$ and Co_2MnGa both exhibit large AHA with $\tan\Theta^{H} = 0.2$ ($Co_3Sn_2S_2$) [4] and 0.12 (Co_2MnGa) [8]. Antiferromagnetic (AFM) half-Heusler materials such as GdPtBi [9] and TbPtBi [10] also display a large intrinsic AHE with $\tan\Theta^{H}$ values as large as 0.16-0.76 [9-12]. Although these materials harbor Weyl nodes induced by magnetic fields, their large AHE does not originate from Weyl nodes but arises from the large net Berry curvature produced by the anticrossing of spin-split bands near the Fermi level [9,12]. Besides the large AHE caused by the presence of anticrossing Weyl nodes or bands, recent studies show that

gapped nodal rings can also generate extremely large AHE [13,14]. This was experimentally demonstrated in FM Heusler Co_2MnAl [14], whose AHA reaches a record value with $\tan\Theta^H = 0.21$ at room temperature. In addition, the non-collinear AFM structure can lead to a large Berry curvature, resulting in a large intrinsic AHE [15,16]; this has been seen in a range of AFM topological materials with broken TRS, such as Mn_3Sn [17] and Mn_3Ge [18].

In this paper, we report a surprisingly large AHE in the Pd-based half-Heusler compound TbPdBi. Its $\tan\Theta^H$ value reaches ~ 2, which is the largest among all known magnetic topological materials. Our in-depth theoretical analysis suggests that such an extremely large AHE originates from a half-topological semimetal (HTS) state. HTS is a long-sought topological state in materials and it can be viewed as a topological version of the half-metallic state in which electrons conduct in only one spin channel, while the other spin channel is insulating [19-21]. Since such a state could generate low-power-consuming spin current, it holds great promise for applications in topological quantum spintronic devices [22]. Moreover, it has been theoretically shown that a gap opening at the non-trivial band crossing points transforms the HTS into a quantum anomalous Hall insulator [23,24]. These exotic properties have inspired extensive interest and a variety of material systems have been predicted to be HTSs, such as two-dimensional(2D) MnN [25], PrOBr [26], and $PtCl_3$ [24]; quasi-1D X_2RhF_6 (X=K, Rb, Cs) [27] and XYZ_3 (X=Cs, Rb, Y=Cr, Cu, Z=Cl, I) [28]; 3D MF_3 (M=Pd, Mn) [29], LiV_2F_6 [30], among others. The Dirac/Weyl points or nodal rings in all these materials are comprised of spin-polarized bands [21,30,31]. However, these theoretical predictions are still awaiting experimental verification. Our work here demonstrates that TbPdBi hosts a unique HTS in proximity to a topological critical point. Such a peculiar HTS in TbPdBi results in not only an unusually large AHE but also leads to a giant negative magnetoresistance. Additionally, we find that the Hall resistivity of TbPdBi exhibits a distinct anomalous peak in the

low-field range, where its isothermal magnetization depends nearly linearly on field. This behavior can be understood in terms of the Berry curvature enhancement induced by spin canting.

b. Results

Single crystals of TbPdBi were grown using the Bi-flux method (Methods). Their temperature dependence of resistivity $\rho_{xx}(T)$ is found to exhibit a broad peak around 50K (supplemental Fig. S1a), indicating their semi-metallic nature. This can be understood as follows: In a semimetal with a small Fermi pocket, high-temperature transport is primarily governed by excited carriers, which results in a semiconducting behavior. In contrast, at low temperatures, excited charge carriers are substantially suppressed, and transport is dominated by the electrons/holes hosted by the small Fermi pocket, resulting in a metallic behavior with a broad peak in $\rho_{xx}(T)$. Magnetic susceptibility (χ) measurements (Fig. S1a) show the AFM state with T_N = 5.2 K. ρ_{xx} exhibits a steeper drop below T_N, indicating the presence of electronic transport coupled with magnetism. We performed a Curie-Weiss (CW) fit for the temperature dependence of susceptibility $\chi(T)$: the best fit was obtained in the temperature range of 100-300K (Fig. S1b), which yields the effective magnetic moment (μ_{eff}) of 9.4 μ_B/Tb, consistent with a prior report [32].

c. Anomalous Hall effect

From Hall resistivity (ρ_{xy}) measurements under high magnetic fields, we observed exceptionally strong AHE in TbPdBi. Figure 1a shows the ρ_{xy} data up to 31T at various temperatures over 1.7-20 K. The most significant feature of this data is that it exhibits a striking peak. This peak occurs below T_N (= 5.2K) and extends to temperatures above T_N but diminishes above 50K (supplementary Note 1 and Figs. S2c and 2d). The peak field is ~ 5T below T_N, and slightly shifts to higher fields with increasing temperature. $\rho_{xy}(B)$ gradually evolves into a linear

field dependence after exhibiting a peak. This occurs above 15T for $T < T_N$; at higher temperatures (e.g. 15K and 20K), due to the shift of the peak to higher field, the linear trend develops at higher fields, with the linear slope remaining similar to its value at low temperatures. Such a distinct peak in ρ_{xy} has never been observed before in any other half-Heusler compound, or a full-Heusler antiferromagnet, or a conventional ferromagnet. As noted above, prior work has shown that the isostructural half-Heusler compound (Gd/Tb)PtBi also exhibits a large AHE [9-12], where the ρ_{xy} data also display anomalous peaks near 4.5T with AHAs maxima reaching values of $\tan\Theta^H = 0.16$-0.76 [9-12]. However, the ρ_{xy} anomalous peak of (Tb/Dy)PtBi is far weaker than that of TbPdBi. For comparison, we have added the ρ_{xy} data of TbPtBi at 1.7K to Fig. 1a. While its weak ρ_{xy} peak near 4.5T can be clearly resolved when the data is zoomed into the field range of 0-9T (Fig. 1(c) in ref. [12]), it is hardly discernible when this data is plotted together with the data of TbPdBi in the field range up to 31T (Fig. 1a), suggesting that the replacement of Pt by Pd leads to essential changes in the band structure, a point to which we will return below. In the field regime where ρ_{xy} exhibits an anomalous peak, the longitudinal resistivity ρ_{xx} displays a drastic decrease, followed by a saturation trend in the high-field range where ρ_{xy} evolves into a linear field dependence, as shown in Fig. 2b, which presents representative ρ_{xx} and ρ_{xy} data at 4K. Note that the anomalous ρ_{xy} peak near 5T is not caused by the ρ_{xx} component which might not be removed from the ρ_{xy} data anti-symmetrizing process; this can be seen clearly from the raw data of ρ_{xy} and ρ_{xx} shown in supplementary Fig. S3 which shows that the ρ_{xx} component in ρ_{xy} is negligibly small. To find whether the unusual field dependences of ρ_{xy} and ρ_{xy} arise from a magnetic transition, we measured the magnetization of TbPdBi up to 35T at various temperatures (Methods). This data (Fig. 1b) indicates the presence of a spin-flop transition near 15T. The saturated magnetic moment of Tb^{3+} in the FM phase is ~8.5μ_B/f.u. at 0.57K, comparable to the effective magnetic moment extracted

from the CW fit (μ_{eff} ~ 9.4 μ_B/Tb). This unusual field dependences of ρ_{xx} and ρ_{xy} are indeed coupled with such a magnetic spin-flop transition. The ρ_{xy} peak as well as the sharp drop of ρ_{xx} are present in the canted AFM state (CAFM), while the linear field dependence of ρ_{xy} and the ρ_{xx} saturation behavior occur in the polarized FM phase. These observations imply that the spin-flop transition leads to an electronic structure transition. We will show below that our theoretical calculations demonstrate that the spin-flop transition in TbPdBi drives an electronic phase transition and gives rise to the HTS state.

Given that the remarkable ρ_{xy} peak is present in the CAFM state, its origin is most likely associated with the Berry curvature induced by the noncolinear spin structure. In general, ρ_{xy} of magnetic systems can be described by $\rho_{xy} = \rho_{xy}^N + R_S M + \rho_{xy}^T$, where the first term is the normal Hall contribution, the second term represents the anomalous Hall resistivity linearly coupled with magnetization M (R_S is the anomalous Hall coefficient), and the last term ρ_{xy}^T is the anomalous Hall resistivity arising from the noncollinear spin structure. The ρ_{xy} peak of TbPdBi in the CAFM state suggests that it involves a significant component of anomalous Hall resistivity $\Delta\rho_{xy}^{AH}(=\rho_{xy} - \rho_{xy}^N)$. At low temperatures with $T \leq T_N$, ρ_{xy}^N can be expressed as $R_0 B$ (R_0 is the normal Hall coefficient), shown as the dashed line in Fig.1(a). If we assume that the spin-flop transition does not lead to a striking change in carrier density, we can extract the approximate $\Delta\rho_{xy}^{AH}$ by subtracting ρ_{xy}^N ($=R_0 B$) from ρ_{xy} (supplementary Note 2 and Fig. S2a). However, when the temperature is above T_N, ρ_{xy}^N deviates from $R_0 B$ and displays noticeable characteristics of multiple-band normal Hall effect for T > 50K due to thermal excitations (supplementary Note 1). Although the ρ_{xy} peak appears to increase in the temperature range $T_N < T < 20$ K, it should not be due to the increase of $\Delta\rho_{xy}^{AH}$ but

arise from the multiple-band effect in the normal Hall resistivity, which is superimposed on the AHE peak. The AHE peak should become weak above T_N and diminish above 50 K where the ρ_{xy} data can be fitted with a two-band model (supplementary Note 1 and Fig. S2c and 2d)).

In order to understand how the magnetization contributes to $\Delta\rho_{xy}^{AH}$, we have plotted $\Delta\rho_{xy}^{AH}$ as a function of magnetization in supplementary Fig. S4. [Note that $\Delta\rho_{xy}^{AH}$ is obtained by subtracting the normal Hall contribution, i.e. the dashed line in Fig. 1a, which is inferred from the high-field linear field dependence of $\rho_{xy}(B)$]. We find that $\Delta\rho_{xy}^{AH}$ strongly deviates from linear dependence on magnetization and exhibits a striking peak, indicating that the anomalous Hall resistivity of TbPdBi involves a significant contribution of ρ_{xy}^{T}. The maximal $\Delta\rho_{xy}^{AH}$ near 5T is ~ 0.6 mΩ-cm for $T < T_N$ (supplementary Fig. S2a), almost 5-15 times larger than that in (Gd/Tb)PtBi [9,12]. From $\Delta\rho_{xy}^{AH}$, we derive anomalous Hall conductivity σ_{yx}^{AH} using $\sigma_{yx}^{AH} = \Delta\rho_{xy}^{AH}/(\rho_{xy}^{2} + \rho_{xx}^{2})$ and AHA as shown in supplementary Fig. S2b and Fig. 1c. The maximal value of $\tan\Theta^{H}$ is ~ 2 at about 15 T and 4 K (Fig.1c), which is surprisingly large compared to other magnetic topological materials, as shown in Fig. 1d, which plots $\tan\Theta^{H}$ versus σ_{yx}^{AH} for TbPdBi and other magnetic topological materials. Such an extremely large AHE in TbPdBi is likely not induced by extrinsic mechanisms such as skew scattering or side jump since the associated Hall angle is usually quite small ($\tan\Theta^{H} < 0.01$) [33,34]. Further, the dependence of σ_{yx}^{AH} on the longitudinal conductivity σ_{xx} in TbPdBi is consistent with an intrinsic AHE (supplementary Note 3). These results suggest that intrinsic mechanisms due to Berry curvature are at play in generating the unusually large AHE in TbPdBi, a point to which we return below. Notably, previous studies have shown that Skyrmion magnetic lattices could also give rise to an anomalous peak in ρ_{xy} (i.e. a topological Hall effect [35]). Compared to the topological Hall effect of a prototype Skyrmion system MnSi, where anomalous

Hall resistivity jump (i.e. ρ_{xy}^{T}) induced by the spin-texture is less than 0.04 μΩ-cm [36], our observed maximal $\Delta\rho_{xy}^{AH}$ value of ~ 0.6 mΩ-cm in TbPdBi is four orders of magnitude larger. This implies that the extremely large AHE in TbPdBi involves a unique mechanism. We will show below that it is associated with a peculiar HTS state.

d. Large negative magnetoresistance

The steep decrease in ρ_{xx} in field regions where ρ_{xy} exhibits an anomalous peak (Fig. 1b) suggests that TbPdBi host a large negative magnetoresistance. Although we observed large negative magnetoresistance in our earlier low-field (≤ 9T) measurements on TbPdBi [37], its origin remained mysterious; it was also unclear whether its magnetoresistance saturates at high fields. With access to high-field measurements and theoretical analyses, we are in a position to address this issue here. Figures 2a-2b present the transverse and longitudinal magnetoresistivities [MR = $\frac{\rho_{xx}(B)-\rho_{xx}(0)}{\rho_{xx}(0)}$] of TbPdBi measured with the current applied perpendicular and parallel to the magnetic field, respectively, at various temperatures (insets to Fig. 2a and 2b). [Note that these data were measured on the same sample which was used for the Hall resistivity measurements shown in Fig. 1a.] Both transverse and longitudinal MRs decrease steeply with increasing magnetic field, and tend to saturate above 15T; magnitude of the negative MR reaches ~98% as the field rises to 15T. This giant negative MR is observed at both $T \leq T_N$ and $T > T_N$, where the magnitude of the MR remains nearly temperature independent below 20K, but gradually decreases with increasing temperature above 20K (Fig. 2c). Even as the temperature rises to 200K, the negative MR remains significant, with its magnitude being ~ 20% at 9T (Fig. 2c). The MR changes from negative to positive only at room temperature, with the magnitude of the positive MR being much smaller than that of the negative MR at lower temperatures. Since TbPdBi is a superconductor

with T_c = 1.7K, its MR measured at 1.7K (base temperature of our measurement system) first shows a steep increase as the superconducting state is suppressed by magnetic field, followed by a steep decrease as discussed above (supplementary Fig. S5; this data is not included in Fig. 2a-2b for simplicity). Note that giant negative MR observed in TbPdBi does not occur in the isostructural compounds (Gd/Tb/Dy)PtBi [10-12,38,39], which again suggests that TbPdBi hosts an electronic state that is distinct from (Gd/Tb/Dy)PtBi.

Negative MR that has been observed in various materials originates from several different mechanisms. In topological Weyl semimetals, the topological current induced by the chiral anomaly can lead to a large negative MR when the magnetic field is parallel to the current, as observed in GdPtBi [11,38] and TbPtBi [10,12]. When the magnetic field is rotated away from the current, the chiral anomaly is gradually suppressed so that the sign of MR can change from negative to positive above a certain value of the rotation angle. Prior studies have also shown that materials with macroscopic disorders may display negative longitudinal MR, as for example in polycrystalline $Ag_{2+\delta}Se$ [40], gallium arsenide quantum wells [41], and disordered topological insulator $TlBi_{0.15}Sb_{0.85}Te_2$ [42]. Another mechanism involves spin-scattering suppression driven by spin flip/flop transition; an example is the colossal MR in $Ca_3Ru_2O_7$ [43]. None of the aforementioned mechanisms, however, is relevant to our observation of the giant negative MR in TbPdBi. This is because (i) our observed negative MR is nearly independent of field orientation and tends to saturate in the high-field regime, which excludes the chiral anomaly effect, (ii) our samples are high-quality single crystals and do not involve macroscopic disorders, and (iii) the giant negative MR of TbPdBi occurs at both $T \leq T_N$ and $T > T_N$. If this giant negative MR were due to the spin-scattering suppression in the spin-flop transition, we would expect the value of the MR to significantly drop as the spin-flop transition is suppressed at $T > T_N$, which is inconsistent with

the observation of the temperature independence of MR between T_N and 20K and the survival of large negative MR in a wide temperature region above 20K (Fig. 2c). Notably, a large negative transverse/longitudinal MR was recently reported in $EuMnSb_2$ [44] and EuB_6 [45]. The large negative MR in $EuMnSb_2$ is ascribed to the field-induced metal-insulator transition, while the large negative MR of EuB_6 is suggested to arise from the high spin polarization of charge carriers in a half-Weyl semimetal [45]. As discussed below, our band structure calculations for TbPdBi also reveal a high spin-polarization state, which is caused by a unique FM HTS state close to the topological critical point. Our observed giant negative MR in TbPdBi provides strong support for such a HTS state.

e. Electronic structure and Hall conductivity calculations

To understand the unusual transport properties of TbPdBi, we now present our detailed theoretical analysis. Figures 3a-c show the arrangement of atoms in the nonmagnetic, ferromagnetic (FM) with ordering vector [100], and the A-type AFM state with propagation vector [111] [46]. The high-symmetry nonmagnetic state of TbPdBi is described by the inversion asymmetric space group T_d^2 ($F\bar{4}3m$, No. 216). In the [100] FM state, the symmetry of the lattice reduces to fourfold rotary reflection $\bar{S}_4$, which combines the fourfold rotational and mirror symmetries. The associated band structure is semimetallic as shown in Fig. 3d (without spin-orbit coupling). Importantly, the band structure exhibits a band inversion between Γ_8 (p-type) and Γ_6 (s-type) states reminiscent of half-Heulser materials only in the spin-down channel, whereas the spin-up channel is not inverted. Such a unique band structure with a single-spin-channel band inversion can be closely associated with the half-metallic state of magnets, and for this reason, we call it a HTS. This HTS state can host multiband anticrossing points comprised of opposite spin channels. In the presence of SOC, the band anticrossing points are gapped, inducing a non-zero

Berry curvature field that leads to a large AHE (Fig. 3e). Figure 3f shows the band structure of the A-type AFM state of TbPtBi (ground state). The associated crystalline symmetries are threefold rotational symmetry (C_3) around the [111] direction and spacetime symmetry $\tilde{T} = \left\{T \middle| \frac{1}{2}\frac{1}{2}\frac{1}{2}\right\}$, which combines time-reversal symmetry with half-translation along [111]. The band structure is semimetallic with various band crossings along the $\Gamma - Z$ line and contains band inversions in both spin-channels. This nontrivial band inversion in the AFM state evolves to an HTS state with a single-spin channel band inversion in the presence of the magnetic field, which drives the AFM-to-FM transition. This band structure evolution with the magnetic field can lead to an intermediate spin-canted state with various band anticrossing points and enhance the Berry curvature field and the associated AHE.

We emphasize that the distinct anomalous Hall resistivity peak in TbPdBi occurs near 5T (Fig.1a), where the system is in a spin-canted AFM state. We can expect an additional contribution to the AHE stemming from the canted AFM state. As noted in the introduction, the non-collinear spin texture can induce a large non-vanishing Berry curvature. Since TbPdBi possesses the same magnetic structure as GdPtBi/TbPtBi [46], i.e., the magnetic moments of Tb order ferromagnetically on the (111) planes, but are antiferromagnetically coupled along the [111] direction. When the magnetic field is applied long [100], the magnetic moments will gradually tilt toward [100], resulting in a spin-canted state. A recent theoretical study indicates that, in AFM nodal-line materials $AMnBi_2$ (A=Ca, and Yb), a strong AHE could be induced by weak spin canting, so that the anomalous Hall conductivity keeps growing as the canting angle increases [47]. This suggests that the anomalous Hall resistivity peak near 5T in TbPdBi likely has its origin in the canted spin state formed by Tb^+ ions. Such an interpretation is supported by our Berry curvature calculation for the spin canted state, see below.

To calculate the band structure and anomalous Hall conductivity (AHC) in the spin-canted states of TbPdBi under an external magnetic field, we employ the virtual crystal approximation (VCA) where the AFM and FM states are taken as the end members. The VCA Hamiltonian H_{vca} of the spin canted state is thus defined as follows:

$$H_{\mathrm{vca}} = (1-x)H_{\mathrm{AFM}} + xH_{\mathrm{FM}},$$

where H_{AFM} (H_{FM}) is the Hamiltonian for AFM (FM) phase and x is a tuning parameter that varies from 0 to 1. x = 0 (1) denotes the pure AFM (FM) phase, while $0 < x < 1$ describes the spin-canted states. In the x = 0 ground state, the dominant Berry curvature Ω_{yz} resides on the anticrossing points in the ΓZ direction (Fig. 4a). For x = 0.1 (low external magnetic field), although the strong Berry curvature Ω_{yz} remains on the ΓZ path, finite FM coupling splits the oppositely spin-polarized bands, shifting the Berry curvature hot-spots to distinct energies [Fig. 4b]. In the fully polarized FM phase, the Berry curvature Ω_{yz} around Γ becomes quite small [Fig. 4c]. Calculated AHC for x varying from 0 to 1 as a function of energy is shown in Fig. 4d. The AHC is nearly zero at x = 0 due to Berry curvature cancellation induced by effective $\tilde{T}$ symmetry. A dramatic peak emerges near 0.1 eV above the Fermi level at x = 0.1 because the band splitting caused by breaking both C_3 and $\tilde{T}$ reduces the Berry curvature cancellation. The AHC peak gradually flattens and shifts to a higher energy with increasing x. The negative AHC at the Fermi level grows monotonically from x = 0 to 1, which implies that there are non-zero Berry curvatures away from the Γ point in the spin-canted AFM states.

We consider the doping effect on the AHC across the magnetic transition. For each doping concentration, the chemical potential is determined by fixing the number of occupied states. Positive (negative) doping concentration Δn indicates the number of occupied states above (below)

the original occupied particle number, i.e., $\Delta n = n\text{-}n_0$, where n (n_0) is the doped (original) occupied particle number per formula unit cell. When $\Delta n = 0.0085$/f.u., σ_{yz} reaches a maximum near $x = 0.1$, as shown in Fig. 4e, in qualitative agreement with our experimental observations (Fig.1a). Note that σ_{yz} grows dramatically, while σ_{xy} and σ_{zx} remain close to zero, which can be attributed to the anisotropy of the calculated anomalous Hall conductivity (supplementary Note 4). Note also that the simplistic VCA model we used here cannot be expected to quantitatively capture the evolution of magnetic states under an external magnetic field. Indeed, our calculated AHC is seen to be smaller than the experimental value (Fig. S2b), indicating that effects other than those captured by our VCA calculations are at play.

f. Discussion

We first discuss the origin of the large Berry curvature in TbPdBi. Figs. 3d-e show the band structure without and with SOC when the magnetic field is applied along [100]. Band degeneracy lifted by exchange interaction are common in Heusler compounds, such as GdPtBi/TbPtBi [9,11,12]. However, the weaker exchange interaction of Tb ions and the nearly zero band inversion strength in TbPdBi lead to smaller band splittings compared to (Gd/Tb)PtBi. As a result, the spin-split bands create a larger number of crossing points near the Fermi level. A small gap opens at the anti-crossing points with SOC, and a large non-vanishing Berry curvature accumulates at these points.

Note that in REPtBi (RE = Gd, Nd), the non-vanishing Berry curvature is induced by the field-induced Weyl state. The number of Weyl nodes and their locations depend on the direction of the applied magnetic field (*B)*. In TbPdBi, our calculations find two pairs of Weyl nodes around Γ in the FM phase for magnetic field applied along the [100] direction; positions of these Weyl

nodes are summarized in supplementary table I. Since these Weyl nodes are far away from the Fermi level, they cannot induce a large AHE. Furthermore, the absence of a chiral anomaly in our magnetotransport measurements indicates that the Weyl nodes do not contribute to the transport properties of TbPdBi. Hence, we conclude that the giant AHC in TbPdBi cannot be attributed to the Weyl state.

A large Berry curvature can also arise from the spin-canted state. Our calculations show that increasing the canting angle widens the band splitting and enlarges the gap at the anti-crossing points, which results in the enhancement of the Berry curvature along the yz direction (Ω_{yz}). The spin-canted state is of course not unique to TbPdBi, and it has also been observed in other half-Heusler compounds such as GdPtBi [9,11], TbPtBi [12], and DyPtBi [39] where the anomalous Hall conductivity and Hall angle are much smaller than in TbPdBi. One may wonder what makes TbPdBi unique. Our band structure calculations give insight by revealing that TbPdBi hosts a distinct topological state: TbPdBi lies at a critical point of the AFM ground state since its band inversion strength is nearly zero. At the field-driven FM state, it evolves into a HTS state, in which its spin-down bands maintain band inversion, while its spin-up bands lose band inversion and become topologically trivial. Notably, a similar state has been predicted in EuB_6 [48], where a large AHE and large negative MR have been recently reported [45]. These results suggest that the HTS state likely plays a crucial role in enhancing the AHE in topological materials. Since the net Berry curvature involves a summation over all the occupied states, the number of bands crossing the Fermi level could affect the Berry curvature cancellation. In general, compounds showing good-metal behavior usually also exhibit a large Berry curvature cancellation, resulting in a small net Berry curvature. However, in some compounds with bad-metal or semimetal behavior, only a few bands cross the Fermi level, which could reduce the possibility of Berry curvature cancellation.

In TbPdBi, the spin-up and spin-down bands are pushed in opposite directions, with a bandgap opening in the spin-up bands, which substantially reduces the number of bands which cross the Fermi level, thus reducing cancellation effects in the Berry curvature.

The exotic HTS state in TbPdBi leads to not only a large AHE but also a giant isotropic negative MR. As spins are polarized near the Fermi level (spin-polarization reaches 40%) under external magnetic field, the spin-down carriers dominate transport in TbPdBi. The spin-scattering is thus significantly suppressed across the spin-flop transition, which leads to a steep resistivity drop with increasing magnetic field. For fields above 15T, spins are fully polarized (Fig. 1b) and the MR saturates. Since we attribute the large negative MR to an exotic 3D band structure, we expect the MR to be insensitive to field orientation, which is what we observe in TbPdBi (Figs. 2a and 2b). The temperature independence of MR(B) between T_N(=5.2K) and 20K (Figs. 2a and 2b) can also be rationalized in terms of the field-induced FM HTS. Although there is not a long-range spin-flop transition above T_N, short-range AFM order should exist above T_N at zero field, so that a crossover-like transition from PM to FM should occur under high magnetic fields, which is indeed seen in the magnetization data at 20K (Fig. 2b). This indicates that the FM HTS can extend to temperatures above T_N under high magnetic fields. However, for temperature above 50K, thermal effects will excite electrons out of spin-up bands, increasing spin-scattering and reduction of the negative MR, much like the results shown in Fig. 2c.

In summary, we have observed an unusual AHE effect with a surprisingly large anomalous Hall angle ($\tan\Theta^H \approx 2$) and a giant negative MR in TbPdBi. Our analysis indicates that these exotic transport properties originate from the unique HTS state of TbPdBi, dominated by the contribution of spin-down bands. The greatly enhanced AHE results from a significantly reduced Berry curvature cancellation between the spin-down and spin-up bands. Spin canting of the AFM state

under magnetic field increases the number of band anticrossing points and widens the gaps, which in turn increase Berry curvature hot spots near the Fermi level and account for the distinct anomalous Hall resistivity peak at low fields. We also find that the HTS state enhances the spin-polarization for the spin-down band in the FM phase, which explains the giant negative MR. Our study unveils a new pathway for generating an extremely large AHE by tuning the electronic structure and the magnetic state in half-Heusler materials. It thus advances the understanding of the interplay between topological state and magnetism and provides strategies for materials design for spintronic and other applications.

g. Methods

a. Single-crystal growth

Single crystals of TbPdBi were synthesized using the Bi-flux method [49]. The starting materials (Tb, Pd, and Bi powders) were mixed with a molar ratio of Tb: Pd: Bi=1:1:20, loaded into Al_2O_3 crucibles, and sealed in quartz tubes under high vacuum. The mixtures of source materials were heated to 1050°C in a crucible furnace and held at this temperature for 48 hours for homogeneous melting, followed by slow cooling down to 700°C at a rate of 3° C /h. Cubic-shaped single crystals of TbPdBi were obtained by removing the excess Bi flux by centrifuging. The inset of the supplementary Fig. S1c shows an image of a typical TbPdBi crystal. The cubic structure and composition of the grown crystals were confirmed by X-ray diffraction (XRD) measurements (supplementary Fig. S1c) and Energy-dispersive X-ray spectroscopy (EDS). The lattice parameter *a* extracted from the XRD pattern from the (001) plane is ~ 6.6360 Å, consistent with the previously reported value (a ~ 6.65310 Å) [37].

b. Magnetotransport and magnetization measurements

Magnetoresistivity and Hall resistivity measurements were performed using a standard six-probe method in a Physical Property Measurement System (PPMS, Quantum Design). The high-field transport measurements were carried out at the National High Magnetic Field Laboratory (NHMFL) in Tallahassee. The magnetoresistivity and Hall resistivity data presented in this paper are obtained after symmetrizing and antisymmetrizing the longitudinal and transverse Hall resistivity data measured at positive and negative magnetic fields, respectively. All the samples used for transport measurements were polished to rectangular shapes with dimensions of ~0.8mm × 0.7mm × 0.2mm, where the polished surfaces were parallel to the (001) plane. The current was applied along the [100] or [001] directions for both the longitudinal resistivity and the Hall resistivity measurements. Magnetization measurements used the National High Magnetic Field Pulsed Field Facility at Los Alamos National Laboratory and a SQUID magnetometer (Quantum Design).

c. Electronic structure calculations

Electronic structure calculations were performed within the density functional theory framework using the Vienna ab-initio simulation package (VASP) based on the projector-augmented wave method [50-52].The generalized gradient approximation (GGA) was employed to include exchange-correlation effects [53]. An on-site Coulomb interaction was added on Tb *f*-electrons within the GGA+U scheme with U_{eff} = 10 eV. A plane wave cut-off energy of 500 eV was used, along with a $11 \times 11 \times 11$ Γ-centered *k*-point mesh to sample the first Brillouin zones of the cubic and trigonal unit cells associated with various magnetic orderings. Spin-orbit coupling effects were included self-consistently. Transport properties were calculated using a first-principles material-specific, effective tight-binding model Hamiltonian generated using the

VASP2WANNIER90 interface [54]. Tb *d* and *f* orbitals, Pd *s*, *p*, and *d* orbitals, and Bi *p* orbitals were included in constructing the Wannier functions.

References:

[1] M. Onoda and N. Nagaosa, Topological Nature of Anomalous Hall Effect in Ferromagnets, Journal of the Physical Society of Japan **71** 1, 19 (2002).

[2] F. D. M. Haldane, Berry Curvature on the Fermi Surface: Anomalous Hall Effect as a Topological Fermi-Liquid Property, Physical Review Letters **93** 20, 206602 (2004).

[3] N. Nagaosa, J. Sinova, S. Onoda, A. H. MacDonald, and N. P. Ong, Anomalous Hall effect, Reviews of Modern Physics **82** 2, 1539 (2010).

[4] E. Liu, Y. Sun, N. Kumar, L. Muechler, A. Sun, L. Jiao, S.-Y. Yang, D. Liu, A. Liang, Q. Xu, J. Kroder, V. Süß, H. Borrmann, C. Shekhar, Z. Wang, C. Xi, W. Wang, W. Schnelle, S. Wirth, Y. Chen, S. T. B. Goennenwein, and C. Felser, Giant anomalous Hall effect in a ferromagnetic kagome-lattice semimetal, Nature Phys **14** 11, 1125 (2018).

[5] Q. Wang, Y. Xu, R. Lou, Z. Liu, M. Li, Y. Huang, D. Shen, H. Weng, S. Wang, and H. Lei, Large intrinsic anomalous Hall effect in half-metallic ferromagnet $Co_3Sn_2S_2$ with magnetic Weyl fermions, Nature Communications **9** 1, 3681 (2018).

[6] A. Sakai, Y. P. Mizuta, A. A. Nugroho, R. Sihombing, T. Koretsune, M.-T. Suzuki, N. Takemori, R. Ishii, D. Nishio-Hamane, R. Arita, P. Goswami, and S. Nakatsuji, Giant anomalous Nernst effect and quantum-critical scaling in a ferromagnetic semimetal, Nature Phys **14** 11, 1119 (2018).

[7] S. N. Guin, K. Manna, J. Noky, S. J. Watzman, C. Fu, N. Kumar, W. Schnelle, C. Shekhar, Y. Sun, J. Gooth, and C. Felser, Anomalous Nernst effect beyond the magnetization scaling relation in the ferromagnetic Heusler compound Co_2MnGa, NPG Asia Materials **11** 1, 16 (2019).

[8] K. Manna, L. Muechler, T.-H. Kao, R. Stinshoff, Y. Zhang, J. Gooth, N. Kumar, G. Kreiner, K. Koepernik, R. Car, J. Kübler, G. H. Fecher, C. Shekhar, Y. Sun, and C. Felser, From Colossal to Zero: Controlling the Anomalous Hall Effect in Magnetic Heusler Compounds via Berry Curvature Design, Physical Review X **8** 4 (2018).

[9] T. Suzuki, R. Chisnell, A. Devarakonda, Y. T. Liu, W. Feng, D. Xiao, J. W. Lynn, and J. G. Checkelsky, Large anomalous Hall effect in a half-Heusler antiferromagnet, Nature Phys **12** 12, 1119 (2016).

[10] R. Singha, S. Roy, A. Pariari, B. Satpati, and P. Mandal, Magnetotransport properties and giant anomalous Hall angle in the half-Heusler compound TbPtBi, Phys. Rev. B **99** 3, 035110 (2019).

[11] C. Shekhar, N. Kumar, V. Grinenko, S. Singh, R. Sarkar, H. Luetkens, S.-C. Wu, Y. Zhang, A. C. Komarek, E. Kampert, Y. Skourski, J. Wosnitza, W. Schnelle, A. McCollam, U. Zeitler, J. Kübler, B. Yan, H. H. Klauss, S. S. P. Parkin, and C. Felser, Anomalous Hall effect in Weyl semimetal half-Heusler compounds RPtBi (R = Gd and Nd), PNAS **115** 37, 9140 (2018).

[12] Y. L. Zhu, B. Singh, Y. Wang, C. Y. Huang, W. C. Chiu, B. K. Wang, D. Graf, Y. B. Zhang, H. Lin, J. W. Sun, A. Bansil, and Z. Q. Mao, Exceptionally large anomalous Hall effect due to anticrossing of spin-split bands in the antiferromagnetic half-Heusler compound TbPtBi, Phys. Rev. B **101** 16 (2020).

[13] Y. Ominato, A. Yamakage, and K. Nomura, Phase Diagram of a Magnetic Topological Nodal Semimetal: Stable Nodal Line in an Easy-Plane Ferromagnet, Journal of the Physical Society of Japan **88** 11, 114701 (2019).

[14] P. G. Li, J. Koo, W. Ning, J. G. Li, L. X. Miao, L. J. Min, Y. L. Zhu, Y. Wang, N. Alem, C. X. Liu, Z. Q. Mao, and B. H. Yan, Giant room temperature anomalous Hall effect and tunable topology in a ferromagnetic topological semimetal Co_2MnAl, NATURE COMMUNICATIONS **11** 1 (2020).

[15] H. Chen, Q. Niu, and A. H. MacDonald, Anomalous Hall Effect Arising from Noncollinear Antiferromagnetism, Physical Review Letters **112** 1, 017205 (2014).

[16] J. Kübler and C. Felser, Non-collinear antiferromagnets and the anomalous Hall effect, EPL (Europhysics Letters) **108** 6, 67001 (2014).
[17] S. Nakatsuji, N. Kiyohara, and T. Higo, Large anomalous Hall effect in a non-collinear antiferromagnet at room temperature, Nature **527** 7577, 212 (2015).
[18] A. K. Nayak, J. E. Fischer, Y. Sun, B. Yan, J. Karel, A. C. Komarek, C. Shekhar, N. Kumar, W. Schnelle, J. Kübler, and others, Large anomalous Hall effect driven by a nonvanishing Berry curvature in the noncolinear antiferromagnet Mn_3Ge, Science advances **2** 4, e1501870 (2016).
[19] X. L. Wang, Proposal for a New Class of Materials: Spin Gapless Semiconductors, Physical Review Letters **100** 15, 156404 (2008).
[20] H. Ishizuka and Y. Motome, Dirac Half-Metal in a Triangular Ferrimagnet, Physical Review Letters **109** 23, 237207 (2012).
[21] R.-W. Zhang, Z. Zhang, C.-C. Liu, and Y. Yao, Nodal Line Spin-Gapless Semimetals and High-Quality Candidate Materials, Physical Review Letters **124** 1, 016402 (2020).
[22] X.-L. Wang, S. X. Dou, and C. Zhang, Zero-gap materials for future spintronics, electronics and optics, NPG Asia Materials **2** 1, 31 (2010).
[23] Y. Li, D. West, H. Huang, J. Li, S. B. Zhang, and W. Duan, Theory of the Dirac half metal and quantum anomalous Hall effect in Mn-intercalated epitaxial graphene, Phys. Rev. B **92** 20, 201403 (2015).
[24] J.-Y. You, C. Chen, Z. Zhang, X.-L. Sheng, S. A. Yang, and G. Su, Two-dimensional Weyl half-semimetal and tunable quantum anomalous Hall effect, Phys. Rev. B **100** 6, 064408 (2019).
[25] S.-S. Wang, Z.-M. Yu, Y. Liu, Y. Jiao, S. Guan, X.-L. Sheng, and S. A. Yang, Two-dimensional nodal-loop half-metal in monolayer MnN, Physical Review Materials **3** 8, 084201 (2019).
[26] L. Jin, X. Zhang, Y. Liu, X. Dai, and G. Liu, Theoretical realization of two-dimensional half-metallicity and fully spin-polarized multiple nodal-line fermions in monolayer PrOBr, Phys. Rev. B **105** 7, 075414 (2022).
[27] L. Jin, X. Zhang, Y. Liu, X. Dai, L. Wang, and G. Liu, Fully spin-polarized double-Weyl fermions with type-III dispersion in the quasi-one-dimensional materials X_2RhF_6 (X=K, Rb, Cs), Phys. Rev. B **102** 19, 195104 (2020).
[28] T. He, Y. Liu, L. Tian, X. Zhang, W. Meng, X. Dai, and G. Liu, Coexistence of fully spin-polarized Weyl nodal loop, nodal surface, and Dirac point in a family of quasi-one-dimensional half-metals, Phys. Rev. B **103** 8, 085135 (2021).
[29] X. Zhou, R.-W. Zhang, X. Yang, X.-P. Li, W. Feng, Y. Mokrousov, and Y. Yao, Disorder- and Topology-Enhanced Fully Spin-Polarized Currents in Nodal Chain Spin-Gapless Semimetals, Physical Review Letters **129** 9, 097201 (2022).
[30] R.-W. Zhang, X. Zhou, Z. Zhang, D.-S. Ma, Z.-M. Yu, W. Feng, and Y. Yao, Weyl Monoloop Semi-Half-Metal and Tunable Anomalous Hall Effect, Nano Letters **21** 20, 8749 (2021).
[31] X.-L. Wang, Dirac spin-gapless semiconductors: promising platforms for massless and dissipationless spintronics and new (quantum) anomalous spin Hall effects, National Science Review **4** 2, 252 (2017).
[32] Y. Nakajima, R. Hu, K. Kirshenbaum, A. Hughes, P. Syers, X. Wang, K. Wang, R. Wang, S. R. Saha, D. Pratt, J. W. Lynn, and J. Paglione, Topological RPdBi half-Heusler semimetals: A new family of noncentrosymmetric magnetic superconductors, Science Advances **1** 5, e1500242 (2015).
[33] S. Onoda, N. Sugimoto, and N. Nagaosa, Intrinsic Versus Extrinsic Anomalous Hall Effect in Ferromagnets, Physical Review Letters **97** 12, 126602 (2006).
[34] T. Miyasato, N. Abe, T. Fujii, A. Asamitsu, S. Onoda, Y. Onose, N. Nagaosa, and Y. Tokura, Crossover Behavior of the Anomalous Hall Effect and Anomalous Nernst Effect in Itinerant Ferromagnets, Physical Review Letters **99** 8, 086602 (2007).
[35] A. Neubauer, C. Pfleiderer, B. Binz, A. Rosch, R. Ritz, P. G. Niklowitz, and P. Böni, Topological Hall Effect in the A Phase of MnSi, Physical Review Letters **102** 18, 186602 (2009).
[36] M. Lee, W. Kang, Y. Onose, Y. Tokura, and N. P. Ong, Unusual Hall Effect Anomaly in MnSi under Pressure, Physical Review Letters **102** 18, 186601 (2009).

[37] H. Xiao, T. Hu, W. Liu, Y. L. Zhu, P. G. Li, G. Mu, J. Su, K. Li, and Z. Q. Mao, Superconductivity in the half-Heusler compound TbPdBi, Phys. Rev. B **97** 22, 224511 (2018).
[38] M. Hirschberger, S. Kushwaha, Z. Wang, Q. Gibson, S. Liang, C. A. Belvin, B. A. Bernevig, R. J. Cava, and N. P. Ong, The chiral anomaly and thermopower of Weyl fermions in the half-Heusler GdPtBi, Nature materials **15** 11, 1161 (2016).
[39] H. Zhang, Y. L. Zhu, Y. Qiu, W. Tian, H. B. Cao, Z. Q. Mao, and X. Ke, Field-induced magnetic phase transitions and the resultant giant anomalous Hall effect in the antiferromagnetic half-Heusler compound DyPtBi, Phys. Rev. B **102** 9 (2020).
[40] J. Hu, T. F. Rosenbaum, and J. B. Betts, Current Jets, Disorder, and Linear Magnetoresistance in the Silver Chalcogenides, Physical Review Letters **95** 18, 186603 (2005).
[41] J. Xu, M. K. Ma, M. Sultanov, Z.-L. Xiao, Y.-L. Wang, D. Jin, Y.-Y. Lyu, W. Zhang, L. N. Pfeiffer, K. W. West, K. W. Baldwin, M. Shayegan, and W.-K. Kwok, Negative longitudinal magnetoresistance in gallium arsenide quantum wells, Nature Communications **10** 1, 287 (2019).
[42] O. Breunig, Z. Wang, A. A. Taskin, J. Lux, A. Rosch, and Y. Ando, Gigantic negative magnetoresistance in the bulk of a disordered topological insulator, Nature Communications **8** 1, 15545 (2017).
[43] M. Zhu, J. Peng, T. Zou, K. Prokes, S. D. Mahanti, T. Hong, Z. Q. Mao, G. Q. Liu, and X. Ke, Colossal Magnetoresistance in a Mott Insulator via Magnetic Field-Driven Insulator-Metal Transition, Physical Review Letters **116** 21, 216401 (2016).
[44] C. Yi, S. Yang, M. Yang, L. Wang, Y. Matsushita, S. Miao, Y. Jiao, J. Cheng, Y. Li, K. Yamaura, Y. Shi, and J. Luo, Large negative magnetoresistance of a nearly Dirac material: Layered antimonide $EuMnSb_2$, Phys. Rev. B **96** 20, 205103 (2017).
[45] J. Shen, J. Gao, C. Yi, Q. Zeng, S. Zhang, J. Yang, X. Zhang, B. Wang, J. Cong, Y. Shi, X. Xu, Z. Wang, and E. Liu, Dynamic Band-Folding Induced Giant Unconventional Anomalous Hall Effect in Magnetic Weyl Semimetal EuB6, arXiv e-prints, arXiv:2106.02904 (2021).
[46] O. Pavlosiuk, X. Fabreges, A. Gukasov, M. Meven, D. Kaczorowski, and P. Wiśniewski, Magnetic structures of REPdBi half-Heusler bismuthides (RE = Gd, Tb, Dy, Ho, Er), Physica B: Condensed Matter **536**, 56 (2018).
[47] C. Le, C. Felser, and Y. Sun, Design strong anomalous Hall effect via spin canting in antiferromagnetic nodal line materials, Phys. Rev. B **104** 12, 125145 (2021).
[48] S. Nie, Y. Sun, F. B. Prinz, Z. Wang, H. Weng, Z. Fang, and X. Dai, Magnetic Semimetals and Quantized Anomalous Hall Effect in EuB_6, Physical Review Letters **124** 7, 076403 (2020).
[49] P. C. Canfield, J. D. Thompson, W. P. Beyermann, A. Lacerda, M. F. Hundley, E. Peterson, Z. Fisk, and H. R. Ott, Magnetism and heavy fermion-like behavior in the RBiPt series, Journal of Applied Physics **70** 10, 5800 (1991).
[50] P. Hohenberg and W. Kohn, Inhomogeneous Electron Gas, Physical Review **136** 3B, B864 (1964).
[51] G. Kresse and J. Furthmüller, Efficient iterative schemes for ab initio total-energy calculations using a plane-wave basis set, Phys. Rev. B **54** 16, 11169 (1996).
[52] G. Kresse and D. Joubert, From ultrasoft pseudopotentials to the projector augmented-wave method, Phys. Rev. B **59** 3, 1758 (1999).
[53] J. P. Perdew, K. Burke, and M. Ernzerhof, Generalized Gradient Approximation Made Simple, Physical Review Letters **77** 18, 3865 (1996).
[54] N. Marzari and D. Vanderbilt, Maximally localized generalized Wannier functions for composite energy bands, Phys. Rev. B **56** 20, 12847 (1997).
[55] L. Ye, M. Kang, J. Liu, F. von Cube, C. R. Wicker, T. Suzuki, C. Jozwiak, A. Bostwick, E. Rotenberg, D. C. Bell, L. Fu, R. Comin, and J. G. Checkelsky, Massive Dirac fermions in a ferromagnetic kagome metal, Nature **555** 7698, 638 (2018).
[56] N. Manyala, Y. Sidis, J. F. DiTusa, G. Aeppli, D. P. Young, and Z. Fisk, Large anomalous Hall effect in a silicon-based magnetic semiconductor, Nature Materials **3** 4, 255 (2004).

[57] X. Cao, J.-X. Yu, P. Leng, C. Yi, X. Chen, Y. Yang, S. Liu, L. Kong, Z. Li, X. Dong, Y. Shi, M. Bibes, R. Peng, J. Zang, and F. Xiu, Giant nonlinear anomalous Hall effect induced by spin-dependent band structure evolution, Physical Review Research **4** 2, 023100 (2022).

Acknowledgments

Z.Q.M. acknowledges the support from NSF under Grants No. DMR 2211327 & DM-1917579. Partial experimental data is based upon research conducted at The Pennsylvania State University Two-Dimensional Crystal Consortium–Materials Innovation Platform (2DCC-MIP), which is supported by NSF Cooperative Agreement No. DMR-2039351. The work at Northeastern University was supported by the Air Force Office of Scientific Research under award number FA9550-20-1-0322 and benefited from the computational resources of Northeastern University's Advanced Scientific Computation Center (ASCC) and the Discovery Cluster. The work at the National High Magnetic Field Laboratory is supported by the NSF Cooperative Agreement No. DMR-1644779 and No. DMR-1157490 and the State of Florida. The work at TIFR Mumbai is supported by the Department of Atomic Energy of the Government of India under Project No. 12-R&D-TFR-5.10-0100.

Author contributions

The crystal growth and transport measurements were carried out and analyzed by Y.L.Z, Y.W., & Z.Q.M. The high magnetic field measurements were carried out by Y.L.Z., D.G. S.H.L., L.J.M., J.C.P. & J. S. The theoretical work was done by C.Y.H., H.L., B.S. & A.B. This work is supervised by Z.Q.M. (experiment) and B.S. and A.B. (theory).

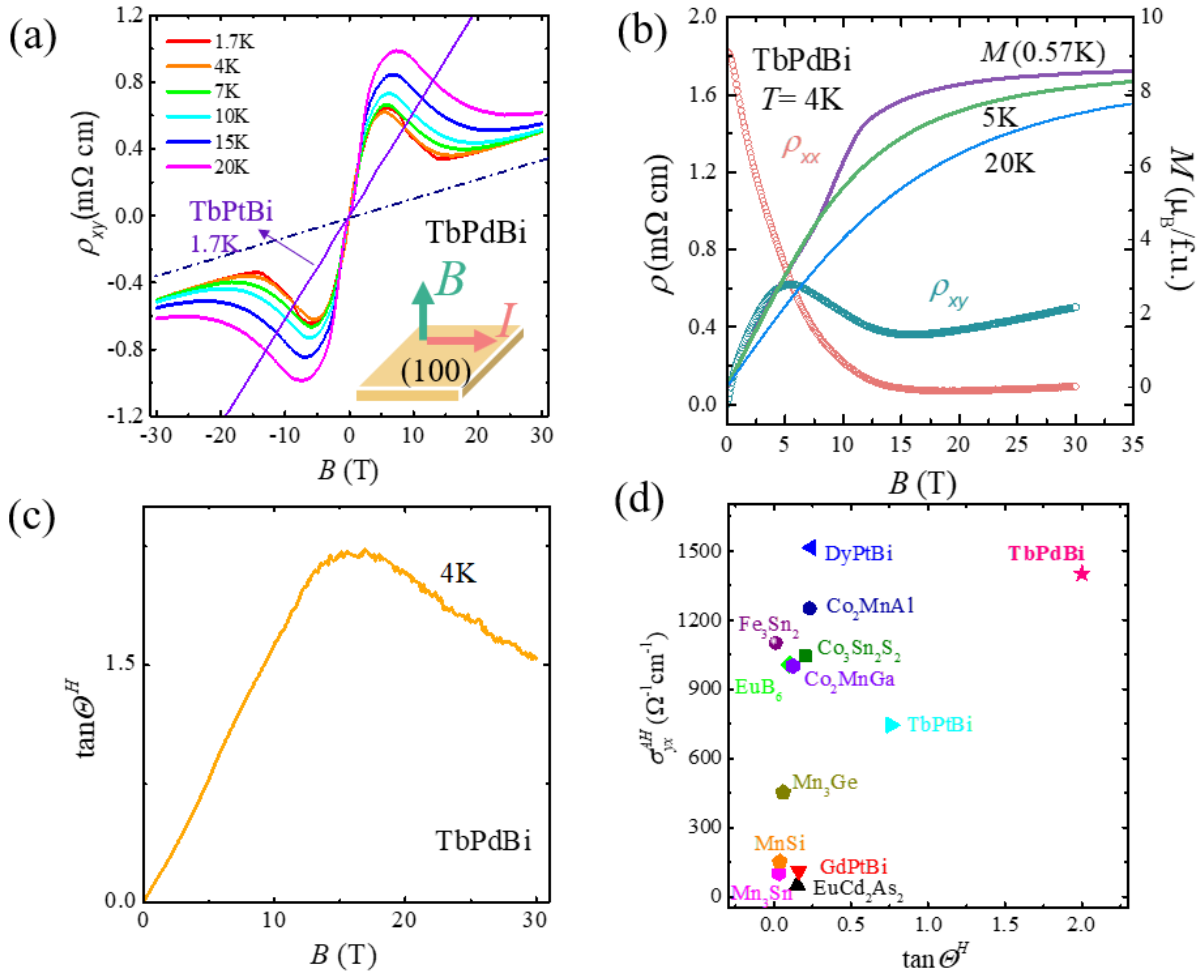

Figure 1. (a) Hall resistivity of TbPdBi as a function of the magnetic field B up to 31T at various temperatures. The Hall data have been anti-symmetrized to remove the minor component of ρ_{xx}. Inset: A schematic of the experimental setup for Hall measurements. (b) Left axis: longitudinal resistivity ρ_{xx} and Hall resistivity ρ_{xy} at 4K for TbPdBi (marked as hollow circles). Right axis: magnetization measured at various temperatures (solid line). (c) TanΘ^H of TbPdBi as a function of magnetic field B at 4K (below Neel temperature). (d) Comparison of σ_{yx}^{AH} and tanΘ^H between TbPdBi and other magnetic conductors [4,6,8,9,12,14,17,18,39,45,55-57].

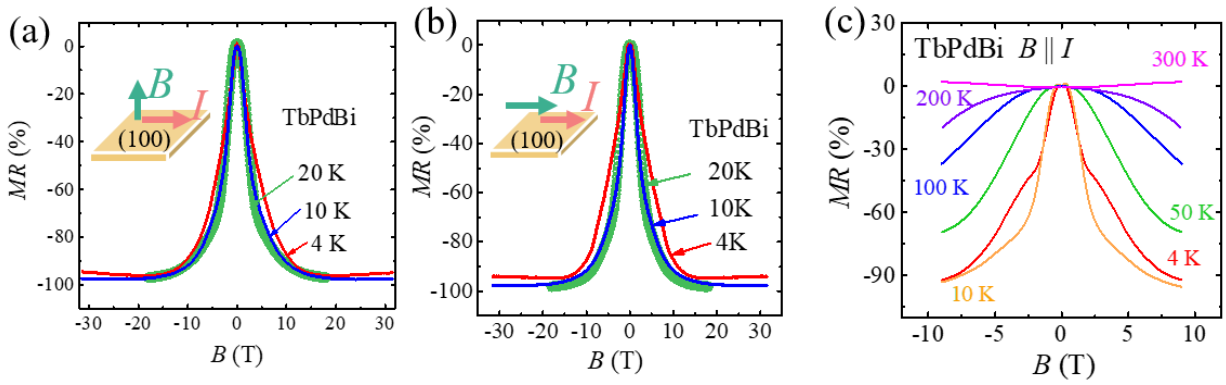

Figure 2. Magnetoresistivity (MR) of TbPdBi: (a-b) Transverse (a) and longitudinal (b) MR = $\Delta\rho/\rho_0 = [\rho(B)–\rho(B=0)]/\rho(B=0)$ at 4K (below Neel temperature), and at 10K and 20K (above Neel temperature). MR at 4K and 10K were measured up to 31T, while the MR at 20K was measured up to 18T. Insets show the schematic of the experimental setup for transverse and longitudinal MR measurements. (c) Longitudinal MR versus magnetic field measured in PPMS at various temperatures.

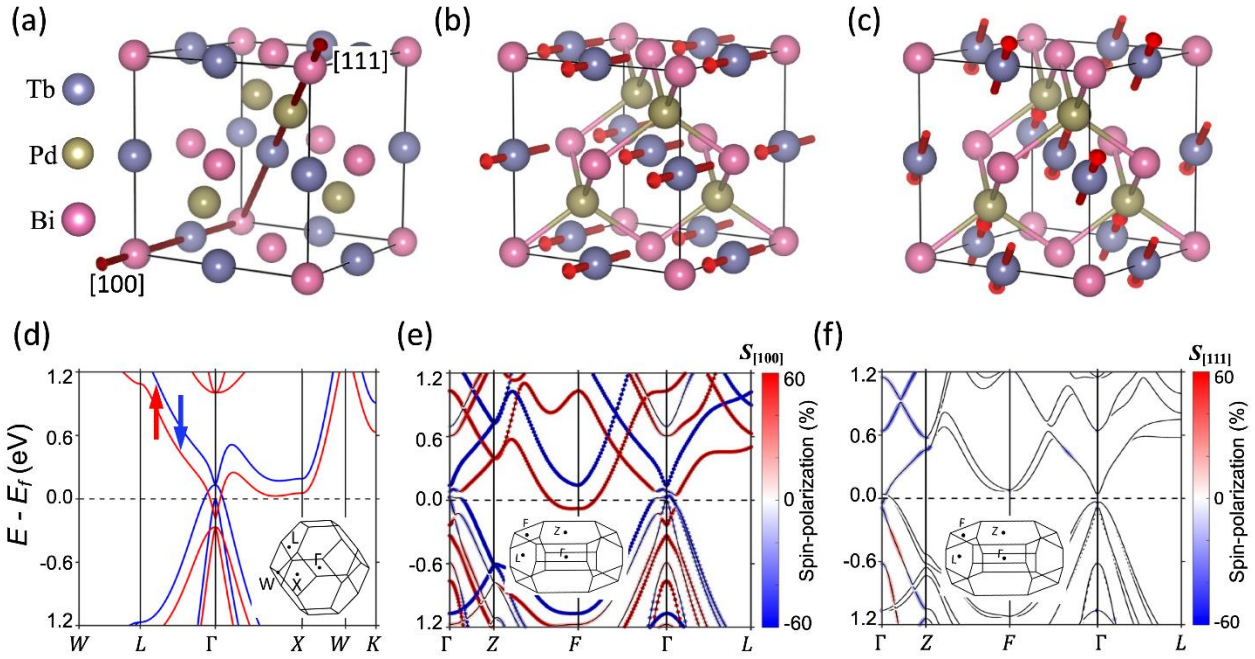

Figure 3. (a) Crystal structure of half-Heusler TbPdBi. [111] and [100] vectors denote the principal magnetic axes for AFM and FM states, respectively. Spin structures of (b) [100] FM and (c) [111] AFM state. Spins are aligned ferromagnetically in a (111) plane and antiferromagnetically between the (111) planes in the AFM state shown in (c). (d) Calculated spin-resolved bulk band structure of FM TbPdBi without SOC. (e) Spin-polarized band structure with SOC in (e) FM and (f) AFM states. Insets in (d)-(e) show the first Brillouin zones associated with the unit cells employed in the calculations.

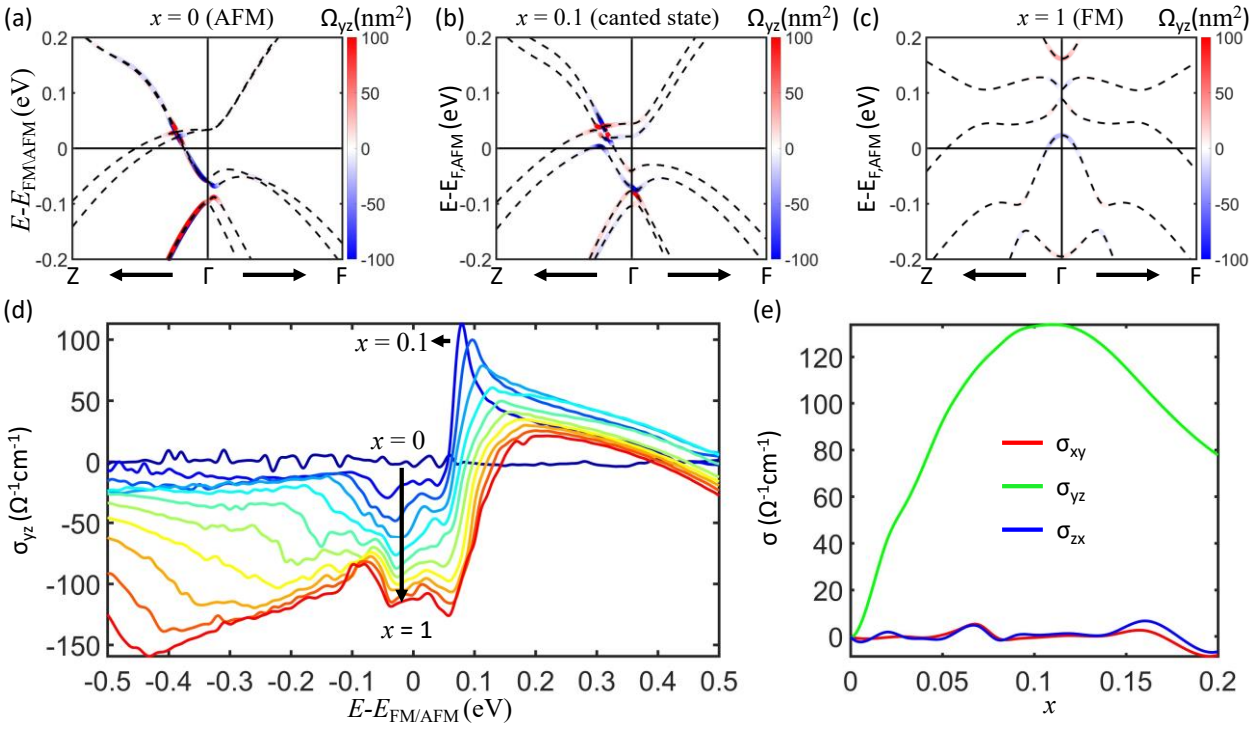

Figure 4. Berry curvature (Ω_{yz}) distribution of TbPdBi band structures for (a) x = 0 (AFM), (b) x = 0.1 (spin-canted state) and (c) x =1 (FM) along high-symmetry directions. (d) Calculated anomalous Hall conductivity (σ_{yz}) as a function of energy for varying x = 0 (dark blue curve) to x = 1 (red curve). (e) Anomalous Hall conductivity as a function of x with Δn = 0.0085/f.u. See text for details.